Supplementary Information

Quantitative Thermal Imaging of Single Walled Carbon Nanotube Devices by Scanning Joule Expansion Microscopy

Xu Xie, [†] *Kyle L. Grosse,* [‡] *Jizhou Song,* [⊥] *Chaofeng Lu,* [§] *Simon Dunham,* [†] *Frank Du,* [†] *Ahmad E. Islam,* [†] *Yuhang Li,* [#]*Yihui Zhang,* [#] *Eric Pop,*[||] *Yonggang Huang,* [#] *William P. King,*[‡,*] *and John A. Rogers*[†,‡,*]

[†]Department of Materials Science and Engineering and Frederick Seitz Materials Research Laboratory,

University of Illinois at Urbana-Champaign, Urbana, Illinois 61801, United States

[‡]Department of Mechanical Science and Engineering

University of Illinois at Urbana-Champaign, Urbana, Illinois 61801, United States

[⊥] Department of Mechanical and Aerospace Engineering,

University of Miami, Coral Gables, Florida 33146, United States

[§] Department of Civil Engineering and Soft Matter Research Center

Zhejiang University, Hangzhou 310058, China

[||]Department of Electrical and Computer Engineering and Micro and Nanotechnology Laboratory,

University of Illinois at Urbana-Champaign, Urbana, Illinois 61801, United States

[#]Department of Mechanical Engineering and Department of Civil and Environmental Engineering,

Northwestern University, Evanston, Illinois 60208, United States

*E-mail: jrogers@uiuc.edu, wpk@illinois.edu

Table of Contents:

1. Details of the SJEM setup

Figure S1 shows a detailed schematic diagram of the scanning Joule expansion microscopy (SJEM) setup. The AFM tip scans the sample surface in contact mode. A laser-photodiode system detects the cantilever deflection caused by intrinsic height variations as well as those due to thermomechanical expansion. A lock-in amplifier operating at the Joule heating frequency captures the expansion signal to form the thermal expansion image. A feedback loop with a cut-off frequency much smaller than the Joule heating frequency processes the topographical signal to form the image and it also controls the piezoelectric stage for scanning[1].

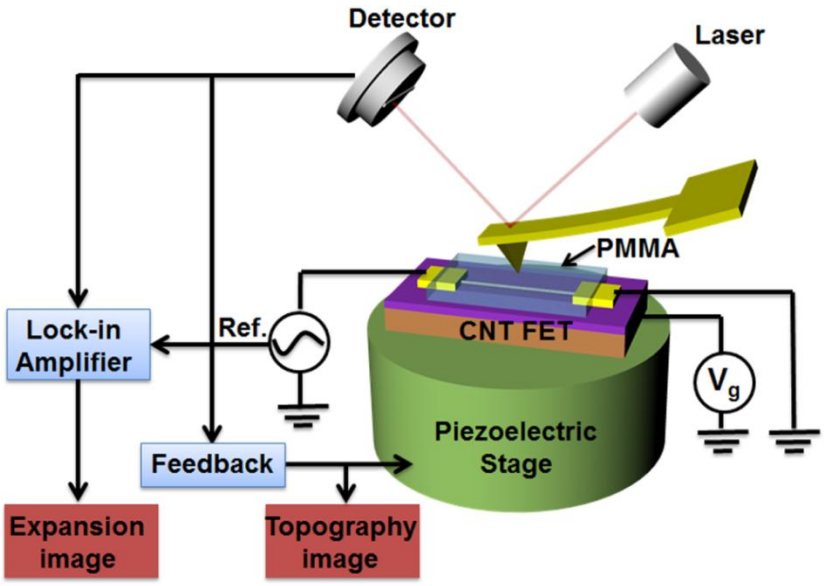

Figure S1. Detailed schematic diagram of the SJEM setup.

2. Details of the two dimensional (2D) analytical model for thermal transport and thermomechanical response

a) Temperature Distribution

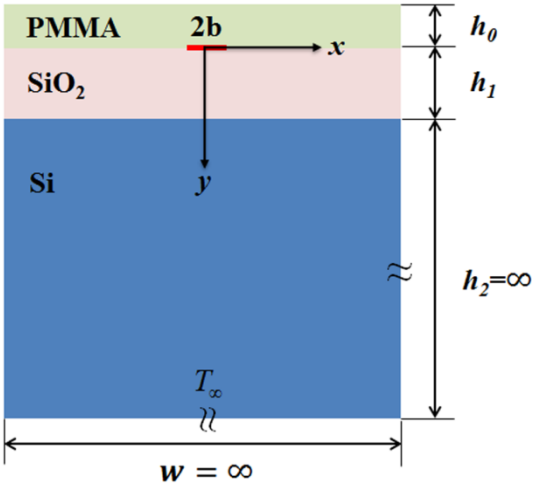

Figure S2. Schematic illustration of the domain for the 2D analytical model

The 2D heat transfer governing equation temperature is

$$\frac{\partial T}{\partial t}-\left(\frac{k}{c\rho}\right)\left(\frac{\partial^2 T}{\partial x^2}+\frac{\partial^2 T}{\partial y^2}\right)=0 \quad (1)$$

where k is thermal conductivity, ρ is density, c is specific heat capacity, and $\alpha = k/(c\rho)$ is thermal diffusivity. In the equations below, the subscripts 0, 1 and 2 denote PMMA, SiO_2 and Si, respectively. Setting $\theta = T - T_\infty$, where T_∞ is the ambient temperature, the above equation is equivalent to

$$\frac{\partial \theta}{\partial t}-(\frac{k}{c\rho})(\frac{\partial^2 \theta}{\partial x^2}+\frac{\partial^2 \theta}{\partial y^2})=0 \quad (2)$$

Due to symmetry ($\left.\frac{\partial \theta}{\partial x}\right|_{x=0}=0$), we only focus on the region with $x \geq 0$. The boundary conditions are

(1) $y=-h_0$ (top surface)

$$-k_0\left.\frac{\partial \theta}{\partial y}\right|_{y=-h_0}=0 \quad (3)$$

(2) $y=0$ ($PMMA/SiO_2$ interface)

$$\theta\Big|_{y=0^-} = \theta\Big|_{y=0^+},\ -k_0\frac{\partial\theta}{\partial y}\Big|_{y=0^-} = \begin{cases} P_0 & 0 \le x \le b \\ P_{c0} & b < x < +\infty \end{cases},\ -k_1\frac{\partial\theta}{\partial y}\Big|_{y=0^+} = \begin{cases} P_1 & 0 \le x \le b \\ P_{c1} & b < x < +\infty \end{cases} \quad (4)$$

where $b=\pi r_0/2$ (r_0 is the radius of the SWNT) is the half width of the heat source; P_0 and P_1 is the heat flux from the heat source at the interface, which satisfy $-P_0 + P_1 = \frac{Q}{2b}$, Q is the power dissipation per unit length along the SWNT; P_{c0} and P_{c1} is the heat flux at the interface where no heat source presents, which satisfy $-P_{c0} + P_{c1} = 0$ due to the continuity (note P_{c0} and P_{c1} are included to show the completeness of the boundary condition; they are not needed to obtain the temperature distribution).

(3) $y = h_1$ (SiO_2/Si interface)

$$\theta\Big|_{y=h_1^-} = \theta\Big|_{y=h_1^+} \text{ and } -k_1\frac{\partial\theta}{\partial y}\Big|_{y=h_1^-} = -k_2\frac{\partial\theta}{\partial y}\Big|_{y=h_1^+} \quad (5)$$

(4) $y = h_1 + h_2 \sim \infty$

$$\theta\Big|_{h_1+h_2} = 0 \quad (6)$$

For an applied voltage $V = V_{ds}\cos(\omega t)$ with the angular frequency $\omega = 2\pi f$, the Joule heating power density is $Q = Q_0(1+\cos(2\omega t))$, which has both DC (*i.e.* Q_0) and AC (*i.e.* $Q_0\cos(2\omega t)$) components. In the following, we will obtain the solution for the AC component, which corresponds to the measurements of SJEM. Assuming the alternating temperature rise is $\theta(x,y,t) = \tilde{\theta}(x,y)\exp(2i\omega t)$, we have

$$\frac{\partial^2\tilde{\theta}}{\partial x^2} + \frac{\partial^2\tilde{\theta}}{\partial y^2} - q^2\tilde{\theta} = 0 \quad (7)$$

where $q^2 = \frac{2\omega i}{\alpha}$.

Eq. (7) can be solved *via* the Fourier cosine transform

$$\begin{aligned} \bar{\tilde{\theta}}(s,y) &= \sqrt{\frac{2}{\pi}}\int_0^{+\infty}\tilde{\theta}(x,y)\cdot\cos(sx)dx \\ \tilde{\theta}(x,y) &= \sqrt{\frac{2}{\pi}}\int_0^{+\infty}\bar{\tilde{\theta}}(s,y)\cdot\cos(sx)ds \end{aligned}, \quad (8)$$

we have

$$-(s^2+q^2)\bar{\bar{\theta}}+\frac{\partial^2\bar{\bar{\theta}}}{\partial y^2}=0 \tag{9}$$

Solving the above equation gives

$$\begin{aligned}\bar{\bar{\theta}} &= A\exp(y\sqrt{s^2+q^2})+B\exp(-y\sqrt{s^2+q^2})\\ \frac{d\bar{\bar{\theta}}}{dy} &= A\sqrt{s^2+q^2}\exp(y\sqrt{s^2+q^2})-B\sqrt{s^2+q^2}\exp(-y\sqrt{s^2+q^2})\end{aligned} \tag{10}$$

where A and B are to be obtained from the boundary conditions. The temperature is then obtained by

$$\tilde{\theta}(x,y)=\sqrt{\frac{2}{\pi}}\int_0^{+\infty}\left[A\exp(y\sqrt{s^2+q^2})+B\exp(-y\sqrt{s^2+q^2})\right]\cdot\cos(sx)ds \tag{11}$$

Therefore, the temperature in Fourier space at each layer is obtained as:

PMMA layer: $\bar{\bar{\theta}}_0(s,y)=A_0\exp(y\sqrt{s^2+q_0^2})+B_0\exp(-y\sqrt{s^2+q_0^2})$

SiO_2 layer: $\bar{\bar{\theta}}_1(s,y)=A_1\exp(y\sqrt{s^2+q_1^2})+B_1\exp(-y\sqrt{s^2+q_1^2})$

Si layer: $\bar{\bar{\theta}}_2(s,y)=A_2\exp(y\sqrt{s^2+q_2^2})+B_2\exp(-y\sqrt{s^2+q_2^2})$

With boundary conditions (3)-(6) in Fourier space, we can obtain the temperature at each layer. For example, A_0 and B_0 are given by

$$A_0=\frac{Q_0(\kappa+1)\exp(h_0\sqrt{s^2+q_0^2})\sin(\frac{\pi r_0}{2}s)}{\pi r_0 s\sqrt{2\pi(s^2+q_1^2)}k_1\left[(1-\kappa)\cosh\left(h_0\sqrt{s^2+q_0^2}\right)+(\kappa+1)\frac{k_0\sqrt{s^2+q_0^2}}{k_1\sqrt{s^2+q_1^2}}\sinh\left(h_0\sqrt{s^2+q_0^2}\right)\right]} \tag{12}$$

$$B_0=A_0\exp(-2h_0\sqrt{s^2+q_0^2})$$

where $\kappa=\dfrac{1-\dfrac{k_2}{k_1}\dfrac{\sqrt{s^2+q_2^2}}{\sqrt{s^2+q_1^2}}}{1+\dfrac{k_2}{k_1}\dfrac{\sqrt{s^2+q_2^2}}{\sqrt{s^2+q_1^2}}}\exp(-2h_1\sqrt{s^2+q_1^2})$

The temperature in PMMA layer is then obtained as

$$\tilde{\theta}_0(x,y)=\sqrt{\frac{2}{\pi}}\int_0^{+\infty}A_0\left[\exp(y\sqrt{s^2+q_0^2})+\exp(-y\sqrt{s^2+q_0^2}-2h_0\sqrt{s^2+q_0^2})\right]\cdot\cos(sx)ds \tag{13}$$

b) Thermal Expansion Based on the temperature distribution

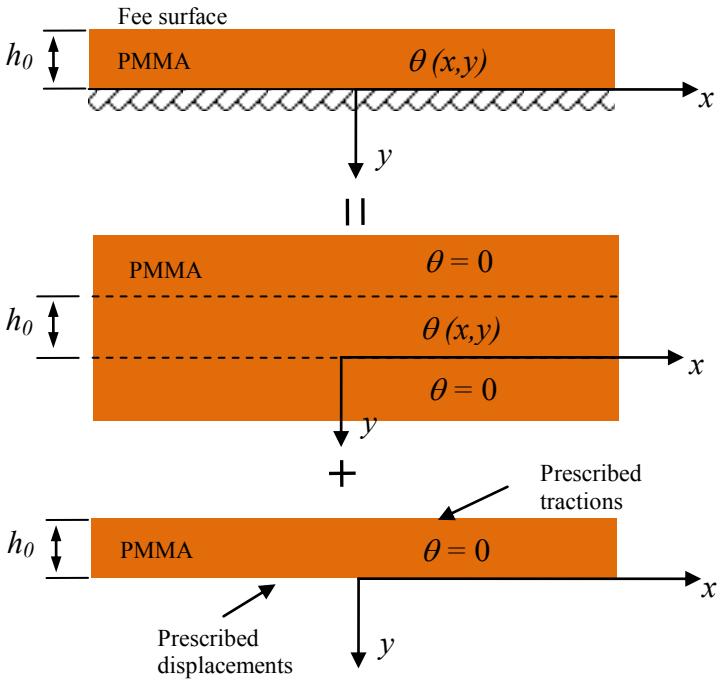

Figure S3. Schematic illustration of the thermo-mechanical model

Only the PMMA layer is considered in calculations of the thermal expansion. Its top surface is traction-free and the bottom surface is fully constrained. The problem is solved by superposing the following two solutions:

(1) Infinite plane with $\tilde{\theta}_0(x,y)$, and

(2) Finite plane without $\tilde{\theta}_0(x,y)$ but with its upper boundary tractions prescribed as the negative of σ_{yy} and σ_{xy} along $y=-h_0$, and the lower boundary displacements prescribed as the negative u and v calculated along $y=0$.

For problem (1), the potential of thermal displacement is given by

$$\psi(x,y)=\frac{1}{2\pi}\frac{1+\nu_0}{1-\nu_0}\beta_0\int_{\xi=-\infty}^{\infty}\int_{\eta=-h_0}^{0}\tilde{\theta}_0(\xi,\eta)\ln\sqrt{(x-\xi)^2+(y-\eta)^2}\,d\xi d\eta \qquad (14)$$

where ν_0 and β_0 are the Poisson ratio and coefficient of thermal expansion (CTE) of PMMA.

The displacements can be obtained

$$u_x = \frac{\partial \psi(x,y)}{\partial x} = \frac{1}{2\pi}\frac{1+\nu_0}{1-\nu_0}\beta_0 \int_{\xi=-\infty}^{\infty}\int_{\eta=-h_0}^{0} \tilde{\theta}_0(\xi,\eta)\frac{x-\xi}{(x-\xi)^2+(y-\eta)^2}\,d\xi d\eta$$
$$u_y = \frac{\partial \psi(x,y)}{\partial y} = \frac{1}{2\pi}\frac{1+\nu_0}{1-\nu_0}\beta_0 \int_{\xi=-\infty}^{\infty}\int_{\eta=-h_0}^{0} \tilde{\theta}_0(\xi,\eta)\frac{y-\eta}{(x-\xi)^2+(y-\eta)^2}\,d\xi d\eta \quad (15)$$

The stresses are given by

$$\sigma_x = -2G_0\frac{\partial^2\psi}{\partial y^2} = -\frac{1}{2\pi}\frac{E_0}{1-\nu_0}\beta_0 \int_{\xi=-\infty}^{\infty}\int_{\eta=-h_0}^{0} \tilde{\theta}_0(\xi,\eta)\frac{(x-\xi)^2-(y-\eta)^2}{\left[(x-\xi)^2+(y-\eta)^2\right]^2}\,d\xi d\eta$$
$$\sigma_y = -2G_0\frac{\partial^2\psi}{\partial x^2} = -\frac{1}{2\pi}\frac{E_0}{1-\nu_0}\beta_0 \int_{\xi=-\infty}^{\infty}\int_{\eta=-h_0}^{0} \tilde{\theta}_0(\xi,\eta)\frac{(y-\eta)^2-(x-\xi)^2}{\left[(x-\xi)^2+(y-\eta)^2\right]^2}\,d\xi d\eta \quad (16)$$
$$\sigma_{xy} = 2G_0\frac{\partial^2\psi}{\partial x\partial y} = -\frac{1}{2\pi}\frac{E_0}{1-\nu_0}\beta_0 \int_{\xi=-\infty}^{\infty}\int_{\eta=-h_0}^{0} \tilde{\theta}_0(\xi,\eta)\frac{2(x-\xi)(y-\eta)}{\left[(x-\xi)^2+(y-\eta)^2\right]^2}\,d\xi d\eta$$

where $G_0 = \frac{E_0}{2(1+\nu_0)}$ is the shear modulus of PMMA and E_0 is the Young's modulus of PMMA. The tractions at $y=-h_0$ are

$$\sigma_y^{h_0} = -\frac{1}{2\pi}\frac{E_0}{1-\nu_0}\beta_0 \int_{\xi=-\infty}^{\infty}\int_{\eta=-h_0}^{0} \tilde{\theta}_0(\xi,\eta)\frac{(h_0+\eta)^2-(x-\xi)^2}{\left[(x-\xi)^2+(h_0+\eta)^2\right]^2}\,d\xi d\eta$$
$$\sigma_{xy}^{h_0} = -\frac{1}{2\pi}\frac{E_0}{1-\nu_0}\beta_0 \int_{\xi=-\infty}^{\infty}\int_{\eta=-h_0}^{0} \tilde{\theta}_0(\xi,\eta)\frac{-2(x-\xi)(h_0+\eta)}{\left[(x-\xi)^2+(h_0+\eta)^2\right]^2}\,d\xi d\eta \quad (17)$$

The displacement at $y=0$ are

$$u_x^0 = \frac{1}{2\pi}\frac{1+\nu_0}{1-\nu_0}\beta_0 \int_{\xi=-\infty}^{\infty}\int_{\eta=-h_0}^{0} \tilde{\theta}_0(\xi,\eta)\frac{x-\xi}{(x-\xi)^2+\eta^2}\,d\xi d\eta$$
$$u_y^0 = \frac{1}{2\pi}\frac{1+\nu_0}{1-\nu_0}\beta_0 \int_{\xi=-\infty}^{\infty}\int_{\eta=-h_0}^{0} \tilde{\theta}_0(\xi,\eta)\frac{-\eta}{(x-\xi)^2+\eta^2}\,d\xi d\eta \quad (18)$$

For problem (2),

Consider the Airy stress function

$$\phi(x,y)=\frac{2}{\pi}\int_0^\infty \bar{\phi}(\xi,y)\cos(\xi x)\,d\xi \tag{19}$$

Substituting the above equations in the biharmonic equation and solving for ϕ, one can obtain

$$\phi(x,y)=\frac{2}{\pi}\int_0^\infty \left[\left(A_1+yA_2\right)e^{-\xi y}+\left(A_3+yA_4\right)e^{\xi y}\right]\cos(\xi x)\,d\xi \tag{20}$$

The stress components are given by

$$\sigma_{xx}=\frac{\partial\phi}{\partial y^2},\sigma_{yy}=\frac{\partial\phi}{\partial x^2},\sigma_{xy}=-\frac{\partial^2\phi}{\partial x\partial y} \tag{21}$$

Combining with the constitutive relation

$$\begin{aligned} e_x &= \frac{1}{E'}\left(\sigma_x-\nu'\sigma_y\right)\\ e_y &= \frac{1}{E'}\left(\sigma_y-\nu'\sigma_x\right)\\ e_{xy} &= \frac{1}{2G}\sigma_{xy} \end{aligned} \tag{22}$$

where $E'=\frac{E_0}{1-\nu_0^{\,2}},\nu'=\frac{\nu_0}{1-\nu_0}$, we can obtain the displacements

$$\begin{aligned} u_x(x,y) &= \frac{2}{\pi}\int_0^\infty \frac{1+\nu_0}{E_0}\left[\xi e^{-\xi y}A_1+\left(-2+2\nu+\xi y\right)e^{-\xi y}A_2+\xi e^{\xi y}A_3+\left(2-2\nu+\xi y\right)e^{\xi y}A_4\right]\sin(\xi x)\,d\xi\\ u_y(x,y) &= \frac{2}{\pi}\int_0^\infty \frac{1+\nu_0}{E_0}\left[\xi e^{-\xi y}A_1+\left(\xi y+1-2\nu\right)e^{-\xi y}A_2-\xi e^{\xi y}A_3-\left(\xi y-1+2\nu\right)e^{\xi y}A_4\right]\cos(\xi x)\,d\xi \end{aligned} \tag{23}$$

where A_1,A_2,A_3 and A_4 can be obtained from

$$\begin{bmatrix} -\xi^2e^{\xi h_0} & \xi^2h_0e^{\xi h_0} & -\xi^2e^{-\xi h_0} & \xi^2h_0e^{-\xi h_0}\\ -\xi^2e^{\xi h_0} & \left(\xi+\xi^2h_0\right)e^{\xi h_0} & \xi^2e^{-\xi h_0} & \left(\xi-\xi^2h_0\right)e^{-\xi h_0}\\ \xi & -2+2\nu & \xi & 2-2\nu\\ \xi & 1-2\nu & -\xi & 1-2\nu \end{bmatrix}\begin{Bmatrix} A_1\\A_2\\A_3\\A_4\end{Bmatrix}=-\begin{Bmatrix} \int_{x=0}^{\infty}\sigma_y^{h_0}\cos(\xi x)\,dx\\ \int_{x=0}^{\infty}\sigma_{xy}^{h_0}\sin(\xi x)\,dx\\ \int_{x=0}^{\infty}\frac{E_0}{1+\nu_0}u_x^0\sin(\xi x)\,dx\\ \int_{x=0}^{\infty}\frac{E_0}{1+\nu_0}u_y^0\cos(\xi x)\,dx \end{Bmatrix} \tag{24}$$

The superposition of problem (1) and problem (2) gives the out-of-plane displacement at $y=-h_0$ as

$$u_y\left(x,y=-h_0\right)=-\frac{1}{2\pi}\frac{1+\nu_0}{1-\nu_0}\beta_0\int_{\xi=-\infty}^{\infty}\int_{\eta=-h_0}^{0}\tilde{\theta}_0\left(\xi,\eta\right)\frac{h_0+\eta}{\left(x-\xi\right)^2+\left(h_0+\eta\right)^2}d\xi d\eta$$
$$\frac{2}{\pi}\int_0^{\infty}\frac{1+\nu_0}{E_0}\left[\xi e^{\xi h_0}A_1+\left(-\xi h_0+1-2\nu\right)e^{\xi h_0}A_2-\xi e^{-\xi h_0}A_3-\left(-\xi h_0-1+2\nu\right)e^{-\xi h_0}A_4\right]\cos\left(\xi x\right)d\xi \quad (25)$$

and its amplitude, which is the value measured by SJEM is $\left|u_y\left(x,y=-h_0\right)\right|$.

c) Thermal Expansion at Low Frequencies

The model in Section 2(b) above is accurate and does not involve any assumptions. At low frequencies, when the thermal diffusion length for PMMA is much larger than the PMMA thickness, the temperature throughout the thickness of PMMA is approximately equal to its surface temperature. Under the assumptions of (1) plane strain in *z* direction because the length of SWNT is much larger than its radius and (2) plane stress in *y* direction because the film is thin and the temperature is thickness independent, the amplitude of the oscillating vertical displacement of the PMMA top surface can be obtained as:

$$\left|u_y\left(x,-h_0\right)\right|=\frac{1+\nu_0}{1-\nu_0}\beta_0 h_0\left|\theta_0\left(x,-h_0\right)\right| \quad (26)$$

where ν_0 and β_0 are the Poisson's ratio and coefficient of thermal expansion (CTE) of the PMMA, respectively. Figure S4 clearly shows that the simple formula is valid for low frequencies (*e.g.*, smaller than 100 kHz, simulated for the case of PMMA thickness 120 nm and SiO_2 thickness 200 nm at Q_0 = 1 μW/μm heating along the SWNT).

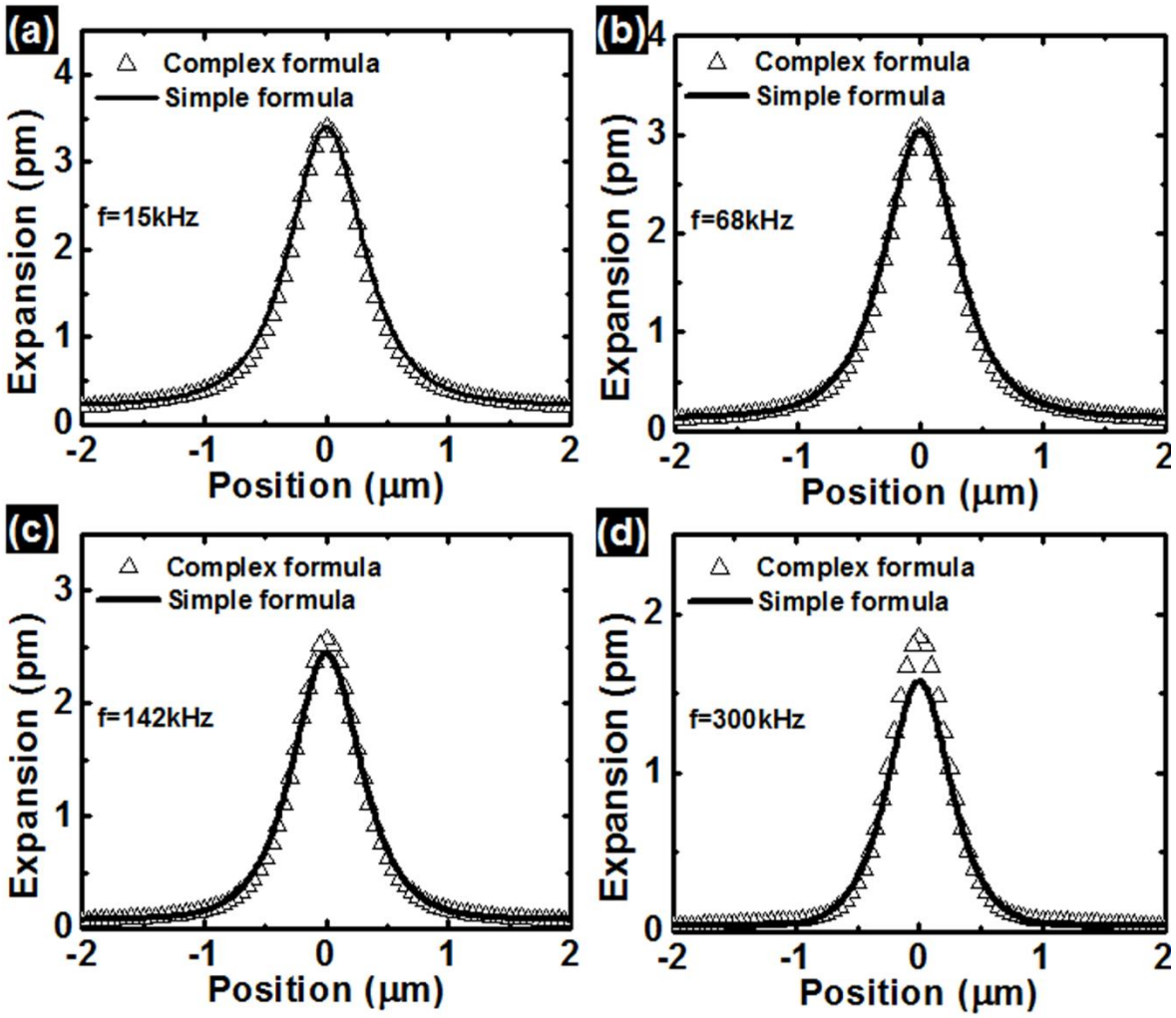

Figure S4. Comparison between the complex formula and the simplified one for (a) f = 15 kHz, (b), 68 kHz, (c) 142 kHz, (d) 300 kHz. Values are simulated for Q_0 = 1 μW/μm with PMMA thickness 120 nm and SiO_2 thickness 200 nm. The simplified formula serves as a good approximation when the frequency is low, *e.g.* <100 kHz for the physical conditions selected here.

3. Properties of the materials used in the analytical model and finite element analysis (FEA)

Table S1. Thermal and Mechanical parameters used in analytical and FE models

Materials	Thermal Conductivity ($Wm^{-1}K^{-1}$)	Thermal Diffusivity 10^{-6} (m^2s^{-1})	Coefficient of Thermal Expansion 10^{-6} (K^{-1})	Young's Modulus 10^9 (Pa)	Poisson Ratio
Si	120 (ref 2)	73	2.6 (ref 3)	165 (ref 4)	0.28 (ref 5)
SiO_2	1.3 (ref 6)	0.84 (ref 6)	0.50 (ref 7)	64 (ref 4)	0.17 (ref 8)
PMMA	0.19 (ref 9)	0.11 (ref 10)	50 (ref 11)	3.0 (ref 12)	0.35 (ref 13)

Note: Si is Boron doped, with resistivity ~0.005 $\Omega \cdot cm$.

4. Additional 2D FEA

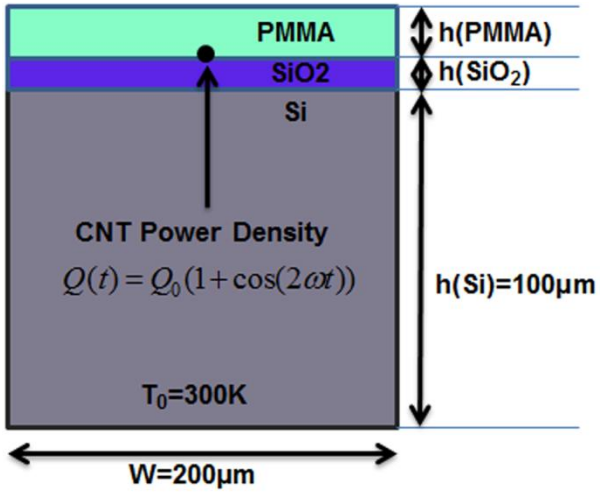

Figure S5. Structure used in the 2D FEA.

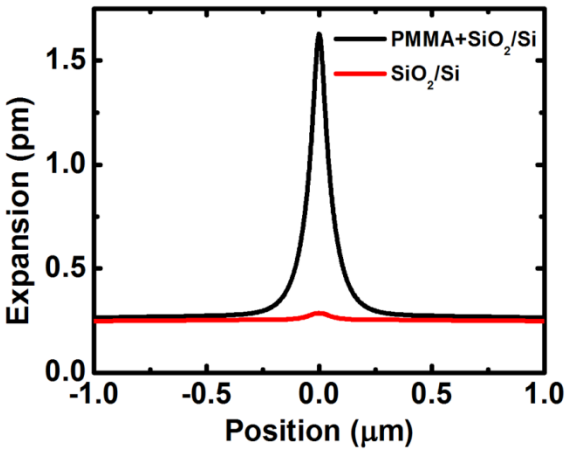

Figure S6. FEA simulation shows the total thermal expansion (black curve, extracted from the top surface of PMMA) and the thermal expansion of SiO_2/Si substrate (red curve). The contribution from SiO_2 is negligible due to very small CTE (~0.5x10^{-6} K^{-1}). Although the Si (CTE ~ 2.6 x10^{-6} K^{-1}) substrate is thick, its temperature rise is insignificant and broadly distributed. Therefore, together, the SiO_2/Si substrate only contributes a nearly flat background to the thermal expansion. The simulation is based on 25 nm PMMA and 90 nm SiO_2, at f = 30 kHz.

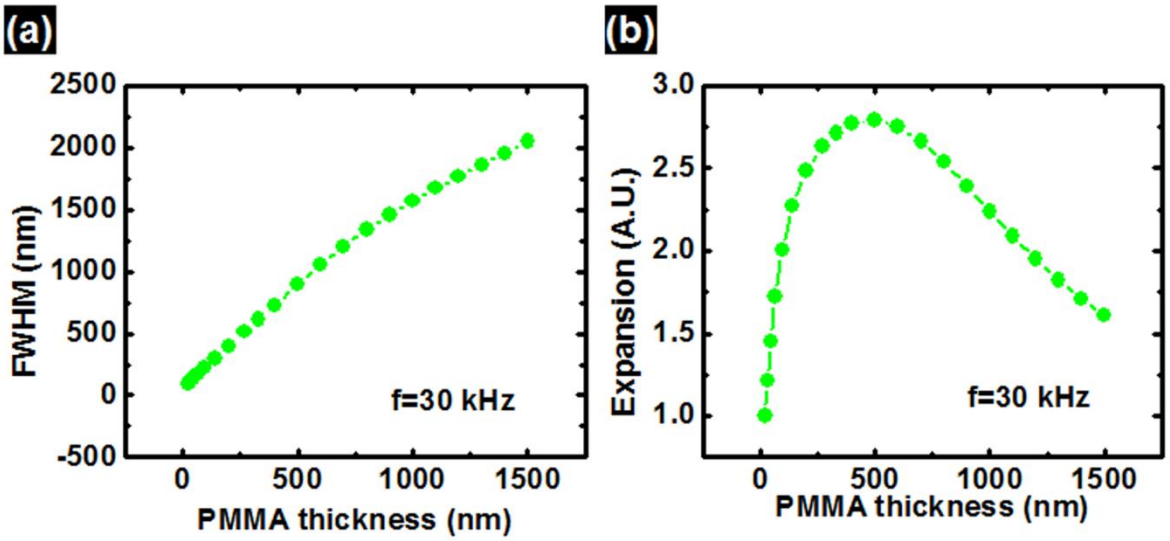

Figure S7. (a) Full width of half maximum (FWHM) for the expansion profiles across the SWNT with PMMA coating ranging from 25 nm to 1500 nm (Values are simulated at f = 30 kHz and SiO_2 thickness = 90 nm). (b) Expansion magnitude for SWNT with constant temperature (Values are simulated under the same conditions as (a)). The signal increases almost linearly with PMMA thickness when the

thickness is small (*e.g.* <100 nm), then reaches a maximum point (at ~500 nm here) and subsequently decreases, as the thermal diffusion length at this frequency becomes larger than the PMMA thickness.

5. Validation of the 2D models

A 3D FEA model was also built to justify the effectiveness of the 2D models. Figure S8a shows the structure used for the simulation. The width is 3 μm and the length of the left and right edges (where no SWNTs are present) are set to be at 2 μm. A SWNT placed at the interface between PMMA (120 nm) and SiO_2 (200 nm) has a diameter of 2 nm and power density of $Q_0 = 1\,\mu\text{W}/\mu\text{m}$. Ignoring the metal electrodes and the silicon substrate simplifies the calculation. Regarding thermal transport, the bottom surface of the structure and the two ends of the SWNT are set to a temperature of 300 K. All other boundary surfaces are thermal insulating and all interfaces are continuous. For calculations of the thermal expansion, the bottom surface is set to be fixed, all other boundary surfaces are free of motion and all the interfaces are characterized by no-slip behavior. Figure S8b shows the typical simulated result, where color represents the temperature and the exaggerated deformation indicates corresponding thermal expansion. Figure S8c shows how the cross-section of thermal expansion (across the center of the SWNT, along Y direction) changes with the length of the SWNT, together with a comparison to results from 2D models. The inset provides a plot of the maximum expansion (*i.e.* expansion value at Y = 0 μm in the cross-section) and its dependence on the lengths of the SWNTs. As the length increases, the magnitude of the cross-section also increases, finally approaching a constant value when L_{SWNT} is larger than about 1 μm (this value for 3D is smaller than that for 2D, because the 3D model here does not include the thick Si substrate, in which case the overall temperature and expansion are underestimated). The results indicate that the power will be overestimated if the 2D model is used for short channel devices (*e.g.* L < 1 μm) due to the effect of the contacts. Figure S8d provides a comparison between the temperature of the SWNT (red curve, here the SWNT is 2 μm) and the maximum thermal expansion on the PMMA surface (black curve), along the length of the SWNT (x direction). The shape of the thermal expansion curve matches the shape of the temperature curve. This

indicates that the 2D models are valid for calculating the temperature distribution along the SWNT (by fitting the cross section of the expansion at each point), with the exception of the regions near the contacts, where the expansion does not accurately reflect the temperature of the SWNT.

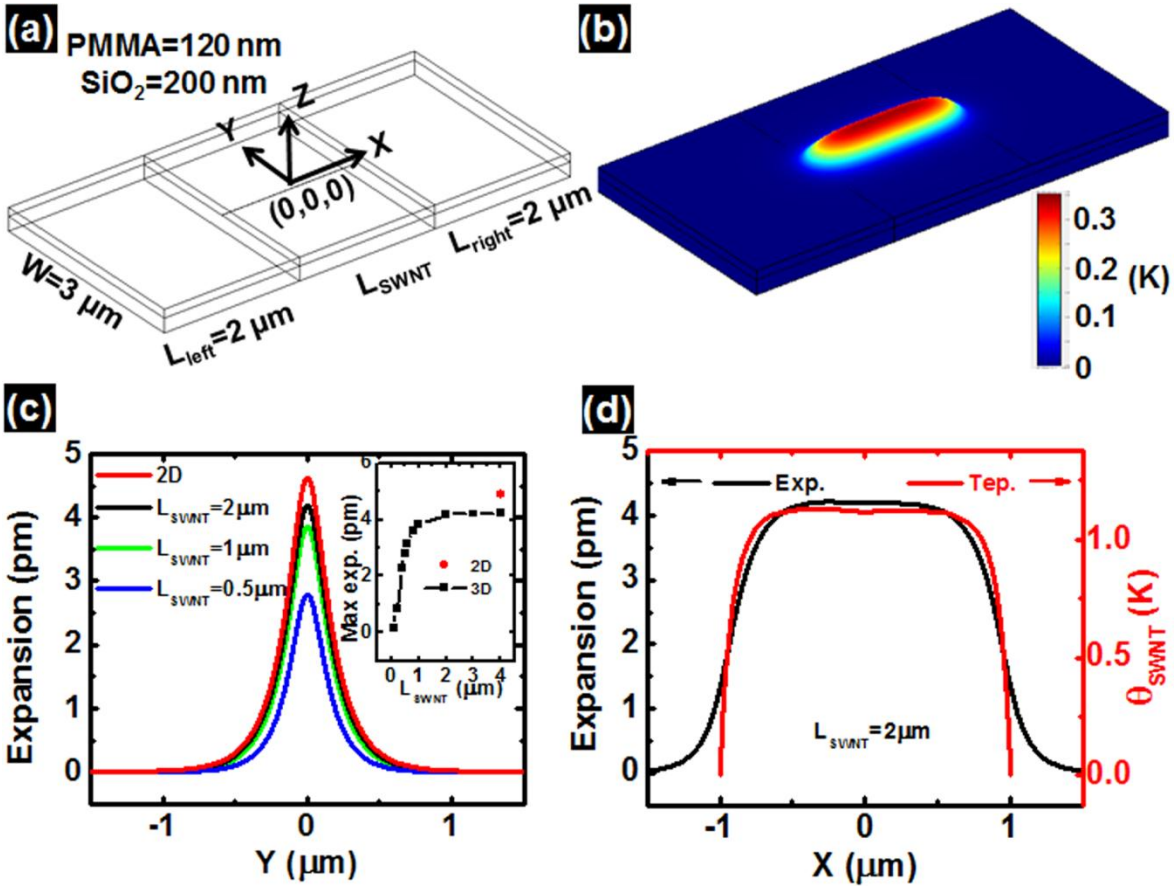

Figure S8. (a) Structure used for the 3D FEA simulation. (b) The result of a 3D simulation, where the color indicates the temperature and the deformation shows the corresponding thermal expansion. (c) Cross-sections of the thermal expansion (across the center of the SWNT, along Y direction) for SWNTs with different lengths, and the comparison with that from the 2D model. The inset shows how the maximum expansion (*i.e.* the point at Y = 0 μm in the cross-section) scales with the lengths of SWNTs. (d) The maximum expansion (black curve) along the length of the SWNT (X direction), and the temperature of the SWNT (red curve). Here the length of the SWNT is fixed as 2 μm.

Moreover, as a particular consideration, the SWNT shown in Figure 3 has a joint where two segments of distinct temperature merge. The 2D analysis near this location has some inaccuracies due to non-

uniformities in the temperature. To evaluate these errors, we note that the thermal transport characteristics at the joint region and the contact regions are essentially the same, *i.e.* both regions show temperature changes from one constant value to another constant value, and the transition distance is characterized by thermal transfer length L_T . Therefore, the analysis associated with Figure S8d not only reflects the errors caused by 2D analysis for the contact region, but the joint region as well.

To further understand the approximation, we solved the thermal transport equation along this SWNT,

$$kA\frac{\partial^2\theta(x,t)}{\partial x^2}+Q_0\cos(2\omega t)-(1/(\frac{1}{g_{\text{int}}}+\frac{1}{g_{sur}}))\theta(x,t)=\rho CA\frac{\partial\theta(x,t)}{\partial t} \qquad (27)$$

Here the SWNT is considered as of two segments, with input power density of Q_0=3.9 μW/μm, length~1.7 μm, diameter~1 nm for one segment and Q_0 = 1.7 μW/μm, length~4.1 μm, diameter~1.2 nm for the other one. The power and length are chosen to match the power density distribution and the total length of the SWNT; all boundary conditions and other physical parameters are the same with the 2D simulation described in the main text. In detail, the joint of the two segments are considered to have continuous heat flux and temperature change; Contacts of the SWNT are kept at room temperature. Thermal conductivity of SWNT k is 3000 W/m/K; $g_{\text{int}}=2\pi r_0 h$ ($h=1.5\times10^8\ \text{W/m}^2\text{/K}$) and g_{sur} □ $0.74W/m/K$ are the same with the 2D model. This 1D analytical treatment has been widely used for understanding the thermal transport along SWNTs.[14-17] As shown in figure S9, the resulting profile from the modeling matches fairly well with the one obtained from 2D analysis of the SJEM results (*i.e.* Figure 3f). As expected, per the discussion above, some similar inaccuracies exist at the contact and joint regions.

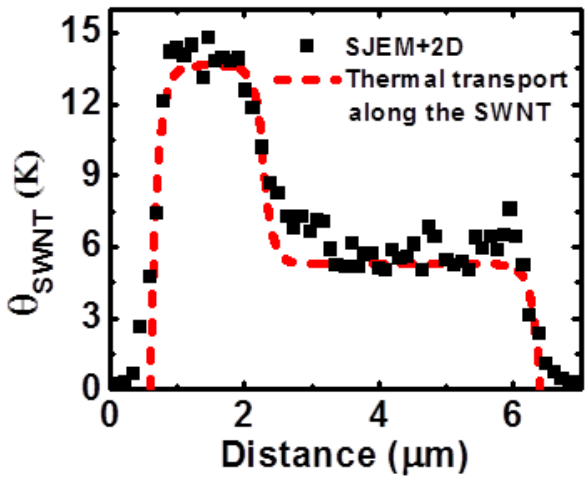

Figure S9. Comparison between the temperature profile (red dashed line) from solving the thermal transport equation along the SWNT and the one from 2D analysis (black solid square) of the SJEM results. Note most parts of the two profiles matches well except for those at the joint region and the contact regions, where similar differences exist.

6. Tip-sample interaction and the resonant enhancement effect

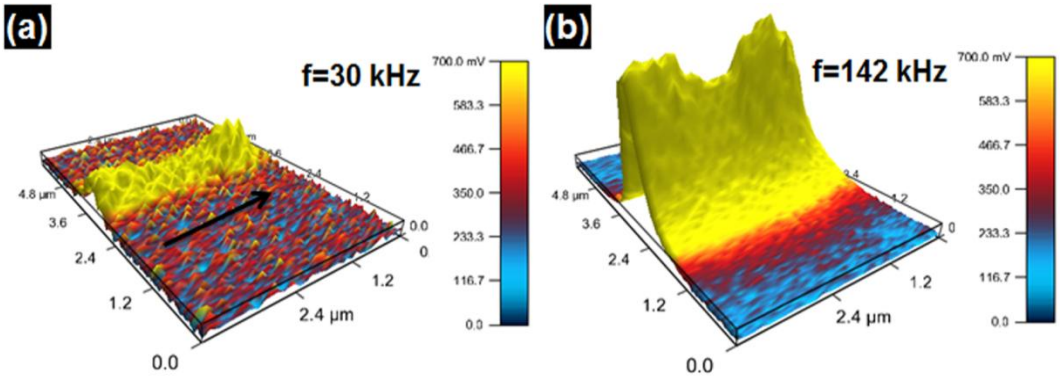

Figure S10. Expansion images from a portion of a SWNT (arrow indicates the direction along the SWNT) collected at (a) f = 30 kHz, and (b) f = 142 kHz, respectively. The same voltage (V_{ds} = 3 V) is used for the Joule heating. The z axis in both images is set at the same scale for purposes of comparison. The image at 142 kHz shows much larger signal (~11 times) than that from 30 kHz due to contact resonance enhancement.

The tip-sample interaction can be captured in a simple way with a damped harmonic oscillator model (with driving frequency of 2ω), where the amplitude of the cantilever A_c can be related to that of the surface A_s according to: [18-20]

$$A_c = A_s \frac{\omega_0'^2 - \omega_0^2}{\omega_0'^2} \frac{1}{\sqrt{(1-4\omega^2/\omega_0'^2)^2 + 4\omega^2\omega_0^2/\omega_0'^4 Q_{AFM}{}^2}} \qquad (28)$$

where w_0 and w_0' are the free resonant frequency and resonance frequency that accounts for the tip-sample interaction (ie. contact resonant frequency), respectively, and Q_{AFM} is the quality factor. When $\omega \ll \omega_0'$, then $A_c = A_s \frac{\omega_0'^2 - \omega_0^2}{\omega_0'^2} \approx A_s$. In our setups, $\omega_0' \approx 300\ kHz$, which is much larger than $\omega_0 \approx 75\ kHz$, such that the cantilever deflection is almost identical to the sample expansion in this low frequency regime. Operating at high frequency can enhance the signal, with a maximum when the heating frequency matches with the contact resonant frequency ($2\omega \approx \omega_0'$), resulting in $\frac{A_c}{A_s} \approx \frac{\omega_0'}{\omega_0} Q_{AFM}$.

7. Simulation of thermomechanical response for point defects in SWNTs

The heat transport for the SWNTs with point defects can be understood by using a 1D heat diffusion picture. Heat generated at the defect site (total power Q_{def}) will flow along the SWNT and into the surrounding materials (here is PMMA and SiO_2), as shown in figure S11a. The governing equation to solve the temperature rise $\theta(x,t)$ due to the defect heating can be written as:

$$kA\frac{\partial^2\theta(x,t)}{\partial x^2} - (1/(\frac{1}{g_{\text{int}}} + \frac{1}{g_{sur}}))\theta(x,t) = \rho CA\frac{\partial\theta(x,t)}{\partial t} \qquad (29)$$

with boundary conditions $-kA\frac{d\theta(x,t)}{dx}\Big|(x=0) = \frac{Q_{def}e^{2i\omega t}}{2}$ and $\theta\Big|(x=L) = 0$. We represent the oscillating temperature as $\theta(x,t) = \theta_0(x)\exp(2i\omega t)$, and equation (28) can be simplified as:

$$\frac{\partial^2\theta_0(x)}{\partial x^2} - \frac{1}{L_T^2}\theta_0(x) - \frac{2i}{L_D^2}\theta_0(x) = 0 \qquad (30)$$

Where $L_T = \sqrt{kA(1/g_{\text{int}} + 1/g_{sur})}$ is the thermal transfer length and $L_D = \sqrt{\frac{k}{\rho c \omega}}$ is the thermal diffusion length. Equation (30) indicates that both L_T and L_D are constrains for the heat flow along the SWNT. While both of them scales linearly with the square root of the thermal conductivity k, L_T is mainly controlled by interface thermal property and L_D is mainly controlled by frequency.

Under the experimental condition where $L_D >> L_T$ and $L >> L_T$ holds, the temperature can be approximated as:

$$\theta_0(x) = \frac{Q_{def} L_T}{2kA} e^{-x/L_T} \qquad (31)$$

This shows that the temperature along the SWNT decays exponentially from the defect site to the rest of the SWNT, with a characteristic length of L_T. Since the amount of heat flow into the PMMA is proportional to the local temperature, the shape of the expansion profile is also directly related to L_T. Finally, the temperature ratio between the defect and the rest of the SWNT is:

$$\theta_0(0) / \theta_{ave} = \frac{Q_{def}}{2L_T Q_{ave}} \qquad (32),$$

where $\theta_{ave} = Q_{ave}(1/g_{\text{int}} + 1/g_{sur})$ is the temperature of the rest of the SWNT.

Rigorous simulation of the heat transport and expansion with defects relies on the 3D FEA model (see Methods). We used two sets of parameters (Table S2), to yield similar results that match the experimental profiles quite well (Figure S11b is for the profiles along the SWNT and Figure S11c is for the cross-sections perpendicular to the SWNT). Both of the two sets of parameters yield $L_T \sim 40\,\text{nm}$. Although the temperature magnitudes are different (Figure S11d), the temperature ratio between the defect and the rest part of the SWNT are similar (ratio~13), as suggested by the simple 1D analytical model.

Table S2. Physical parameters of SWNTs and interface property

Parameter	Diameter (nm)	Thermal conductivity (W/m/K)	Thermal coupling between the SWNT and surroundings per unit area ($W/m^2/K$)
Set 1	1	700	1.5×10^8
Set 2	1	1200	4.5×10^8

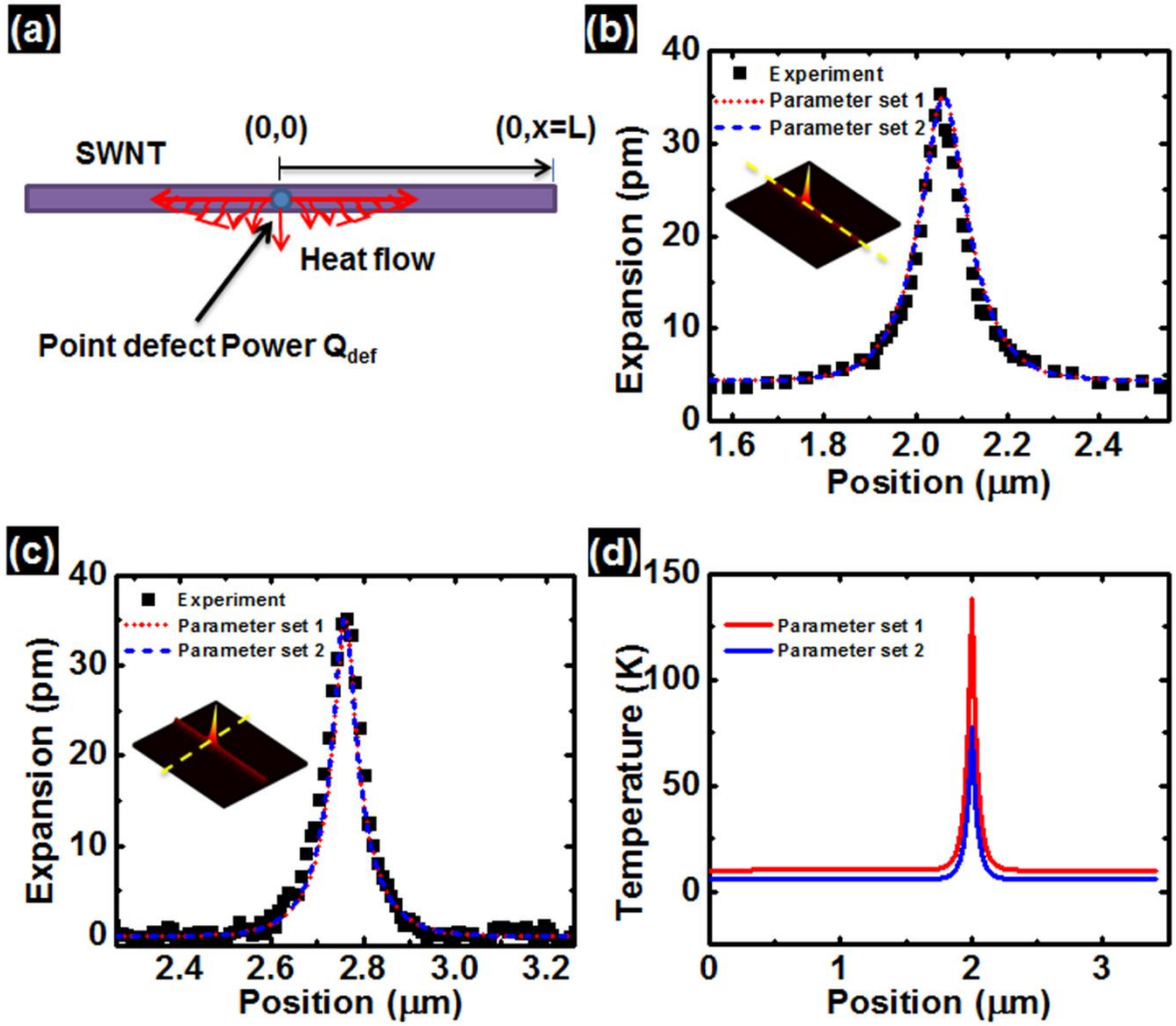

Figure S11. (a) Schematic representation of heat diffusion along the SWNT and heat flow into the surroundings. (b)-(c) Experimental (black solid square) and FEA simulated (red dotted line and blue dashed line) profiles from two sets of different parameters listed in table S2. The yellow dashed line in the inset indicates the location where the profiles are extracted. (d) Simulated temperature distribution along the SWNT for both sets of parameters.

8. Justification of the adiabatic thermal transport boundary condition used at the top surface of the PMMA

To justify the adiabatic boundary condition for the top surface of the PMMA, we calculated both convective and radiative heat losses and compared them with the total input power.

The convective heat loss from the PMMA surface can be described by $Q_C = \int h\theta_{surface} dA$,where h is the coefficient of natural convection (ranging from 5~25 $W/m^2/K$), $\theta_{surface}$ is the temperature rise at the top-surface, and A is the surface area. To do the estimation, we take a typical case shown in figure S12, where $\theta_{surface} \sim 1.5K$ for a given power density $Q_0 \sim 4W/m$. By using the upper bounds of other parameters (width of the temperature profile ~1μm and $h = 25W/m^2/K$), we can get the maximum convective heat loss per unit length along the SWNT as $\sim 3.75\times10^{-5} W/m$, which is about 5 order smaller than the input power density. For other various cases in the experiments, the temperature rise at the top-surface is typically smaller than $1K$ per $1W/m$ (input power), and width of the profile smaller than 2μm. Therefore, we conclude that the convective heat loss can be neglected in our simulations.

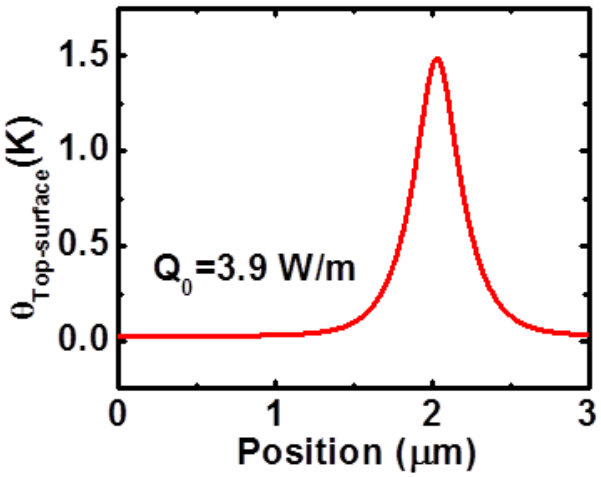

Figure S12. Temperature rise at the top surface of the PMMA, along the cross section marked by dotted lines A from figure 3b. The curve is calculated by FEA simulation, assuming an adiabatic boundary condition of heat transfer at the top surface of the PMMA.

The heat loss due to radiation can be described as $Q_R = \int \sigma[(T_0 + \theta_{surface})^4 - T_0^4]dA$,where $\sigma \sim 5.67 \times 10^{-8} W/m^2/K^4$ is the Stefan-Boltzmann constant and $T_0 = 300K$ is the ambient temperature. Again, doing estimation using $\theta_{surface} \sim 1.5K$ and width of the temperature profile ~1μm, we get the radiation loss~$9.2 \times 10^{-6} W/m$, which is also much smaller than the input power.

Supplementary References:

1. Varesi, J.; Majumdar, A. Scanning Joule Expansion Microscopy at Nanometer Scales. *Appl. Phys. Lett.* **1998**, 72, 37-39.
2. Liu, W. J.; Etessam-Yazdani, K.; Hussin, R.; Asheghi, M. Modeling and Data for Thermal Conductivity of Ultrathin Single-Crystal Soi Layers at High Temperature. *IEEE T. Electron Dev.* **2006**, 53, 1868-1876.
3. Okada, Y.; Tokumaru, Y. Precise Determination of Lattice-Parameter and Thermal-Expansion Coefficient of Silicon between 300-K and 1500-K. *J. Appl. Phys.* **1984**, 56, 314-320.
4. Tada, H.; Kumpel, A. E.; Lathrop, R. E.; Slanina, J. B.; Nieva, P.; Zavracky, P.; Miaoulis, I. N.; Wong, P. Y. Thermal Expansion Coefficient of Polycrystalline Silicon and Silicon Dioxide Thin Films at High Temperatures. *J. Appl. Phys.* **2000**, 87, 4189-4193.
5. Wortman, J. J.; Evans, R. A. Youngs Modulus Shear Modulus and Poissons Ratio in Silicon and Germanium. *J. Appl. Phys.* **1965**, 36, 153-156.
6. Ju, Y. S.; Goodson, K. E. Process-Dependent Thermal Transport Properties of Silicon-Dioxide Films Deposited Using Low-Pressure Chemical Vapor Deposition. *J. Appl. Phys.* **1999**, 85, 7130-7134.
7. Blech, I.; Cohen, U. Effects of Humidity on Stress in Thin Silicon Dioxide Films. *J. Appl. Phys.* **1982**, 53, 4202-4207.
8. Kim, M. T. Influence of Substrates on the Elastic Reaction of Films for the Microindentation Tests. *Thin Solid Films* **1996**, 283, 12-16.
9. Assael, M. J.; Botsios, S.; Gialou, K.; Metaxa, I. N. Thermal Conductivity of Polymethyl Methacrylate (Pmma) and Borosilicate Crown Glass Bk7. *Int. J. Thermophys.* **2005**, 26, 1595-1605.
10. Tsutsumi, N.; Kiyotsukuri, T. Measurement of Thermal-Diffusivity for Polymer Film by Flash Radiometry. *Appl. Phys. Lett.* **1988**, 52, 442-444.
11. Chou, S. Y.; Krauss, P. R. Imprint Lithography with Sub-10 Nm Feature Size and High Throughput. *Microelectron. Eng.* **1997**, 35, 237-240.
12. Ishiyama, C.; Higo, Y. Effects of Humidity on Young's Modulus in Poly(Methyl Methacrylate). *J. Polym. Sci. Pol. Phys.* **2002**, 40, 460-465.
13. Wu, W. L.; Vanzanten, J. H.; Orts, W. J. Film Thickness Dependent Thermal-Expansion in Ultrathin Poly(Methyl Methacrylate) Films on Silicon. *Macromolecules* **1995**, 28, 771-774.
14. Pop, E.; Mann, D. A.; Goodson, K. E.; Dai, H. J. Electrical and Thermal Transport in Metallic Single-Wall Carbon Nanotubes on Insulating Substrates. *J. Appl. Phys.* **2007**, 101, 093710.
15. Xiong, F.; Liao, A.; Pop, E. Inducing Chalcogenide Phase Change with Ultra-Narrow Carbon Nanotube Heaters. *Appl. Phys. Lett.* **2009**, 95, 243103.
16. Shi, L.; Zhou, J. H.; Kim, P.; Bachtold, A.; Majumdar, A.; McEuen, P. L. Thermal Probing of Energy Dissipation in Current-Carrying Carbon Nanotubes. *J. Appl. Phys.* **2009**, 105, 104306.
17. Liao, A.; Alizadegan, R.; Ong, Z. Y.; Dutta, S.; Xiong, F.; Hsia, K. J.; Pop, E. Thermal Dissipation and Variability in Electrical Breakdown of Carbon Nanotube Devices. *Phys. Rev. B* **2010**, 82, 205406.
18. Sarid, D., *Scanning Force Microscopy : With Applications to Electric, Magnetic, and Atomic Forces*. Oxford University Press: New York, 1991; p xi, 253 p.

19. Song, Y. X.; Bhushan, B. Atomic Force Microscopy Dynamic Modes: Modeling and Applications. *J. Phys-Condens. Mat.* **2008**, 20, 225012.
20. Gannepalli, A.; Yablon, D. G.; Tsou, A. H.; Proksch, R. Mapping Nanoscale Elasticity and Dissipation Using Dual Frequency Contact Resonance Afm. *Nanotechnology* **2011**, 22, 355705.